Supporting Information for Publication

Protein-Assisted Assembly of Modular 3D Plasmonic Raspberry-like Core/Satellite Nanoclusters: Correlation of Structure and Optical Properties

Roland P. M. Höller,[1,2] Martin Dulle,[3] Sabrina Thomä,[1] Martin Mayer,[2] Anja Maria Steiner,[2] Stephan Förster,[3] Andreas Fery,[1,2,4,5] Christian Kuttner,[1,2,5] Munish Chanana*[1,6]*

[1]Physical Chemistry II, University of Bayreuth, 95440 Bayreuth, Germany

[2]Leibniz-Institut für Polymerforschung Dresden e.V.,
Institute of Physical Chemistry and Polymer Physics, Hohe Straße 6, 01069 Dresden, Germany

[3]Physical Chemistry I, University of Bayreuth, 95440 Bayreuth, Germany.

[4]Physical Chemistry of Polymeric Materials,
Technische Universität Dresden, Hohe Straße 6, 01069 Dresden, Germany

[5]Cluster of Excellence Centre for Advancing Electronics Dresden (cfaed),
Technische Universität Dresden, 01062 Dresden, Germany

[6]Institute of Building Materials, ETH Zürich, 8093 Zürich, Switzerland.

*Corresponding Author: munish.chanana@uni-bayreuth.de; christian.kuttner@ipfdd.de

UV/vis Characterization of Satellite Particles with Different Protein Coatings

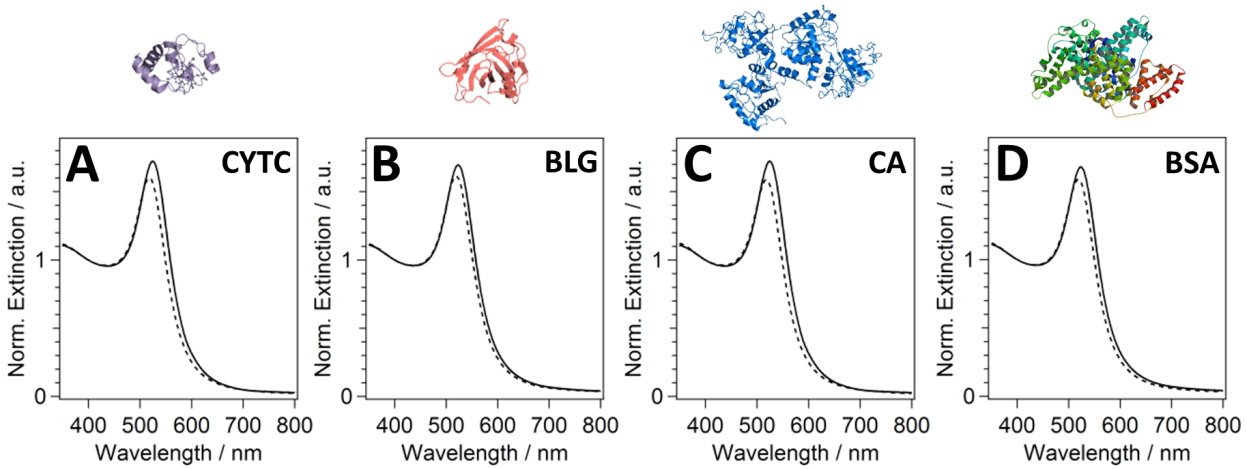

Figure S1: UV/vis of satellite particles before (dashed curve) and after the coating (solid curve) with different proteins: (**A**) cytochrome c from bovine heart (2x Cys, 104 AAs, 11.6 kDa), (**B**) ß-lactoglobulin from bovine milk (5x Cys, 162 AAs, 18.3 kDa), (**C**) conalbumin from chicken egg white (30x Cys, 686 AAs, 75.8 kDa), and (**D**) bovine serum albumin (35x Cys, 583 AAs, 66.4 kDa). The LSPR maxima before/after the coating with CYTC, BLG, CA, and BSA were found to appear at a wavelength of 519/524 nm, 519/524 nm, 519/525 nm, and 519/524 nm, respectively.

Nanoclusters assembled with Different Protein Coatings

Another important tool for fine-tuning the optical properties of nanoclusters is the coverage degree (*i.e.,* the average number of satellite NPs adsorbed on one core NP). In contrast to the modularity in size and composition, tuning the interparticle distances and the relative geometry of building blocks in such 3D assemblies is in general more challenging. In general, the coverage degree strongly depends on the interactions between the core and satellite NPs, which again depend on the physico-chemical parameters such as pH, ionic strength, size and concentration ratios of core and satellite NPs, and their mixing rate. Remarkably, the choice of the protein used for satellite coating, which functions as the "glue" in the assembly, also influences the coverage degree, and thus the final optical properties of the nanoclusters.

Figure S2 shows the influence of the protein on nanocluster formation in respect to surface coverage. Different proteins, namely cytochrome C from bovine heart (CYTC), ß-lactoglobulin from bovine milk (BLG), conalbumin from chicken egg-white (CA) and BSA were investigated for the formation of homometallic core/satellite nanoclusters with gold cores of 71 nm in diameter and gold satellites of 16 nm.

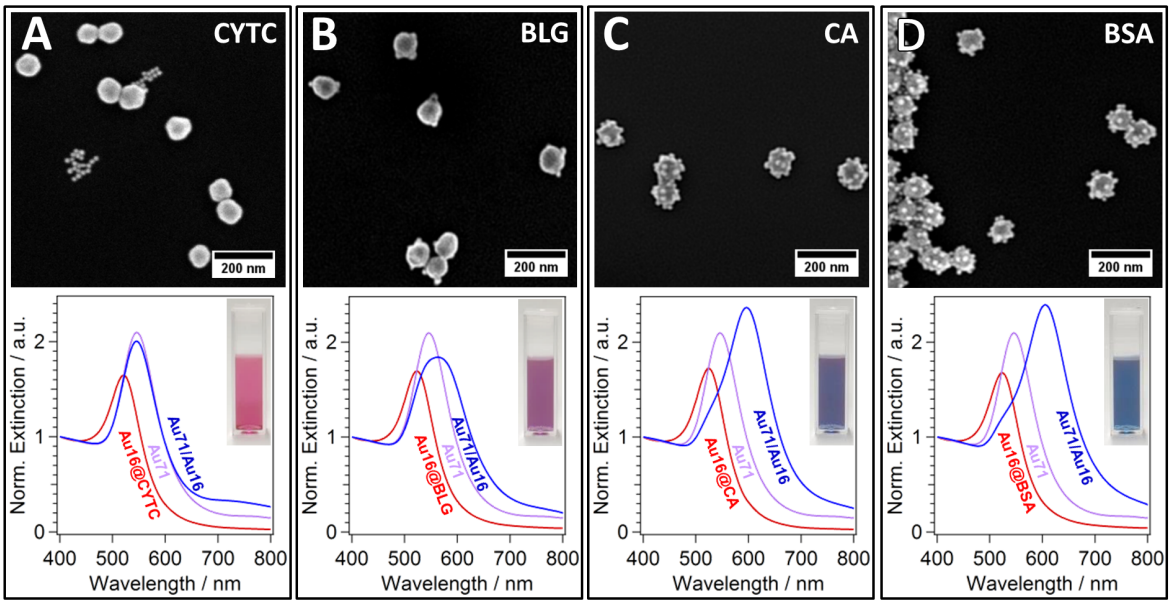

Figure S2: Nanoclusters with low and high surface coverage of satellites. SEM images (top) and UV/vis spectra (bottom) of homometallic core/satellite nanoclusters with gold cores of 71 nm in diameter and gold satellites of 16 nm in diameter coated with different proteins: (**A**) CYTC, (**B**) BLG, (**C**) CA, and (**D**) BSA, respectively.

We found that the selected proteins strongly differ in their ability to form core/satellite nanoclusters (see **Figure S2)**, while keeping the above-mentioned physico-chemical parameters constant (see **Experimental Section**). However, the formed nanoclusters are highly stable over long periods of storage (see **Figure S3)**.

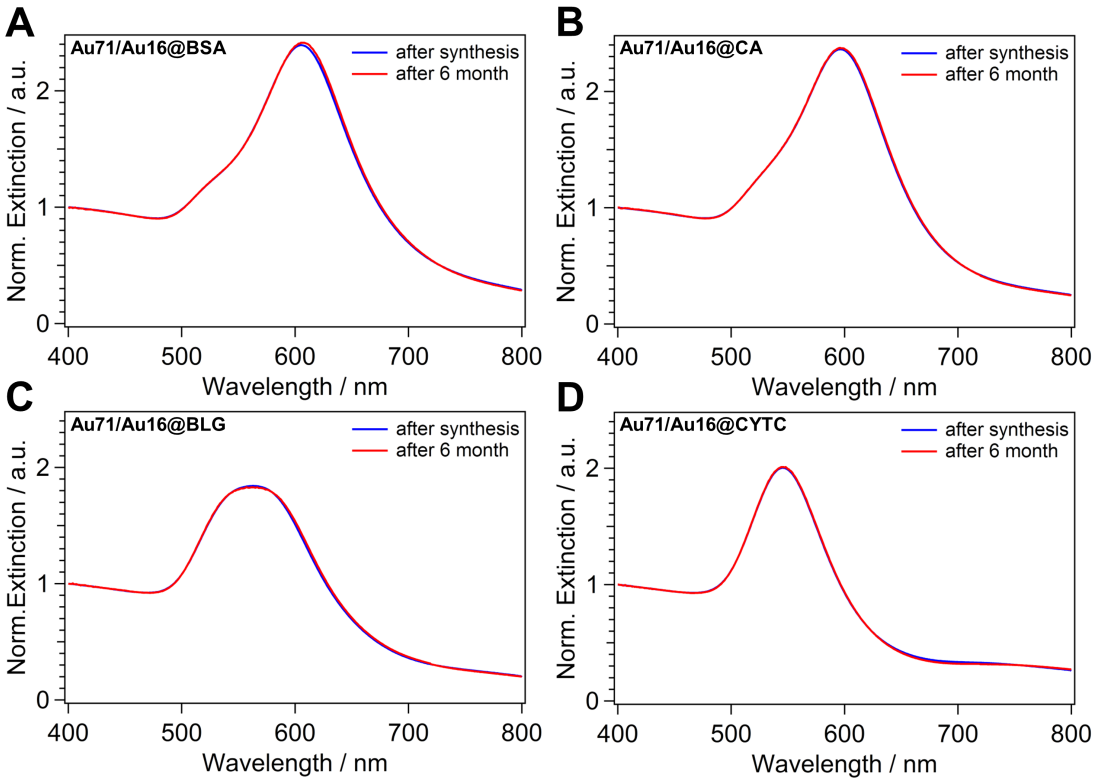

Figure S3: Comparison of UV/vis spectra of core/satellites nanocluster samples after synthesis and after 6 months upon storage in a fridge: (A) Au71/Au16@BSA, (B) Au71/Au16@CA, (C) Au71/Au16@BLG, and (D) Au71/Au16@BSA demonstrating the long-term stability of the nanoclusters.

The proteins were chosen according to their molecular weight (MW) and the abundance of thiol/disulfide groups, *i.e.*, the relative content of the amino acid (AA) cysteine (RCC, #cysteines / #AAs), with CYTC (12.2 kDa,[1] RCC 1.9%) showing the lowest relative content, followed by BLG (18.4 kDa,[1] RCC 3.1%), CA (77.8 kDa,[2] RCC 4.3%), BSA (66.4 kDa,[3] RCC 6.0%), and insulin (5.8 kDa,[4] RCC 11.8%) with the highest relative content. Furthermore, all selected proteins exhibited a negative net charge under the cluster formation conditions at pH 10.[5] CYTC, with the relative cysteine content (RCC) of 1.9% did not lead to a notable nanocluster formation, as suggested by electron microscopy (**Figure S2A,** top) and confirmed by the optical response (no LSPR shift, **Figure S2A,** bottom) and the unaltered color of the dispersion (color almost identical to the bare core NPs, **Figure S2A**, inset). On the other hand, insulin with a highest RCC, but smallest MW also did not lead to cluster formation (no LSPR shift, **Figure S4**).

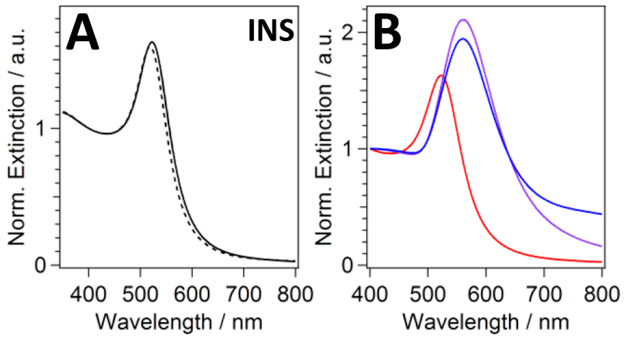

Figure S4: (**A**) UV/vis of satellite particles before (dashed curve) and after the coating (solid curve) with insulin recombinant human (6x Cys, 51 AAs, 5.8 kDa). The LSPR maxima before/after the coating with insulin were found to appear at a wavelength of 519/524 nm, respectively. (**B**) UV/vis of a homometallic core/satellite nanocluster dispersion (blue curve) assembled from ~95 nm citrate-stabilized Au cores (violet curve, LSPR maximum: 561 nm) and ~15 nm insulin-coated Au satellites (red curve). Despite the high relative cysteine content (RCC) of insulin (11.8%), insulin-coated satellite AuNPs were found not to be suitable for nanocluster formation (no red-shift of the LSPR). Thus, indicating that besides the RCC of proteins also other parameters as the molecular weight and related with this, the availability of remaining cysteine groups on the protein-coated satellites after the satellite coating step, play an important role for structure formation.

In the case of BLG, with a RCC of 3.1%, only sparsely populated nanoclusters with BLG-coated satellites were obtained. Consequently, only a minor red shift of the radiant mode was realized (see **Figure S2B,** bottom). The two large proteins CA and BSA yield nanoclusters with a relative high coverages of satellite NPs. CA with the RCC of 4.3% shows slightly lower coverage as BSA (RCC 6.0%), as indicated by the less pronounced red-shift of the radiant mode (see **Figure S2C,** bottom). These results suggest that the combination of a high molecular weight and a high relative content of cysteine groups in the protein seems to be important in the formation of nanoclusters with high satellite coverage. Furthermore, the availability of the remaining cysteine groups on the protein-coated satellites may play an important role too, which we assume is very low in the case of insulin, owed to their consumption in the satellite coating step. However, the selected proteins differ completely in their primary structure (*i.e.*, AA sequence), in their molecular weight as well as in their higher structures (secondary, tertiary) and in the flexibility of

the tertiary structure. Therefore, a general law, which holds for all proteins, cannot be drawn from the small selection of studied examples, owing to the complexity of the matter. Besides cysteine, the relative content and the accessibility of AAs with other metal binding functional groups such as amines (lysine, histidine) and carboxylates (aspartate, glutamate), which are also expected to mediate the core/satellite assembly, could be important. Nevertheless, our results show that the choice of protein allows for modulation of the nanocluster configuration (high or low coverage degrees) and thus tailor its optical properties to a certain extent. A systematic study on tuning the interparticle distances and the satellite coverage of nanoclusters is the subject of ongoing work.

UV/vis Characterization of Au and Ag Satellite NPs before and after Coating with BSA

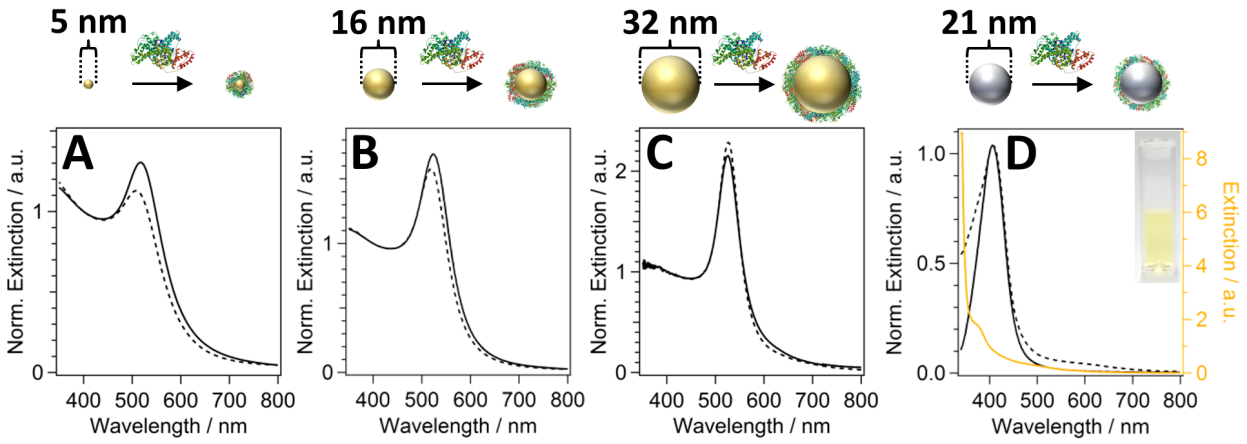

Figure S5: UV/vis spectra of (**A**) 5 nm and (**B**) 16 nm citrate-stabilized and (**C**) 32 nm sized CTAC-stabilized AuNPs (dashed curve) in comparison to the AuNPs after the BSA-coating (solid curve). The LSPR maxima before/after the coating with BSA were found to appear at a wavelength of 509/517 nm, 519/524 nm, and 526/525 nm, respectively. (**D**) UV/vis spectra of 21 nm Ag satellites stabilized by tannic acid/citrate (dashed curve, LSPR maximum: 407 nm) and after the BSA-coating (black solid curve, LSPR maximum: 406 nm). An aqueous solution of tannic acid shows two absorption bands at around 380 nm and 500 nm as well as a steep absorbance increase toward lower wavelengths (orange solid curve, right axis). The inset shows a photograph of the AgNP dispersion after BSA coating.

UV/vis Characterization of the Assembly and Purification of Core/Satellite Nanoclusters

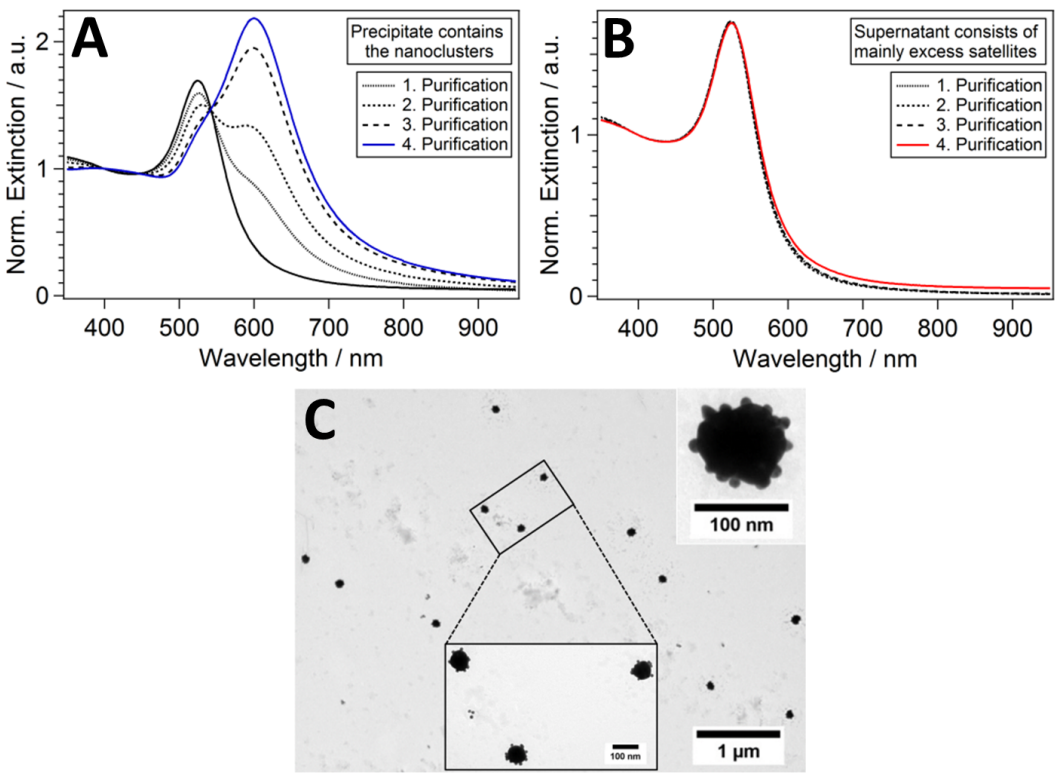

Figure S6: Purification process followed by UV/vis spectroscopy of (**A**) the redispersed precipitate and (**B**) the supernatant of an exemplary assembly of Au84/Au16 core/satellite nanoclusters after different purification cycles. (**C**) TEM images of the resulting nanoclusters consisting of 16 nm satellite and 84 nm core NPs. The TEM images demonstrate that the nanoclusters are freely dispersed colloids that can be randomly deposited on a substrate by drop casting of the diluted dispersion.

Mixing of Non-Assembling Building Blocks (*i.e.*, Citrate-Stabilized Satellites and Cores)

The hybridization model predicts that the nonradiant mode, which accounts for a dominant satellite-to-satellite coupling, always lies in the spectral range between the core and the satellite. The presence of the red-shifted radiant mode clearly evidences a hybridization of core and satellite LSPRs. This mode relies on strong coupling between core and satellite NPs. By simply mixing NPs this effect cannot be achieved. We tested this by mixing 22 nm and 84 nm citrate-stabilized particles (LSPR 521 and 552 nm, respectively) in various mixing ratios. These NPs do not form nanoclusters, since the protein coating on the smaller particles is absent. The mixture is colloidally stable due to the citrate stabilization. Depending on the excess of satellites, the ensemble LSPR is shifted from the LSPR of the large NPs towards the LSPR of the small NPs. **Figure S7** shows an exemplary NP mixture in 1:30 ratio with an ensemble LSPR at 535 nm. The mixtures did not yield the proposed modes characteristic for nanocluster hybridization. Thus, coupling between small and large NPs can be excluded.

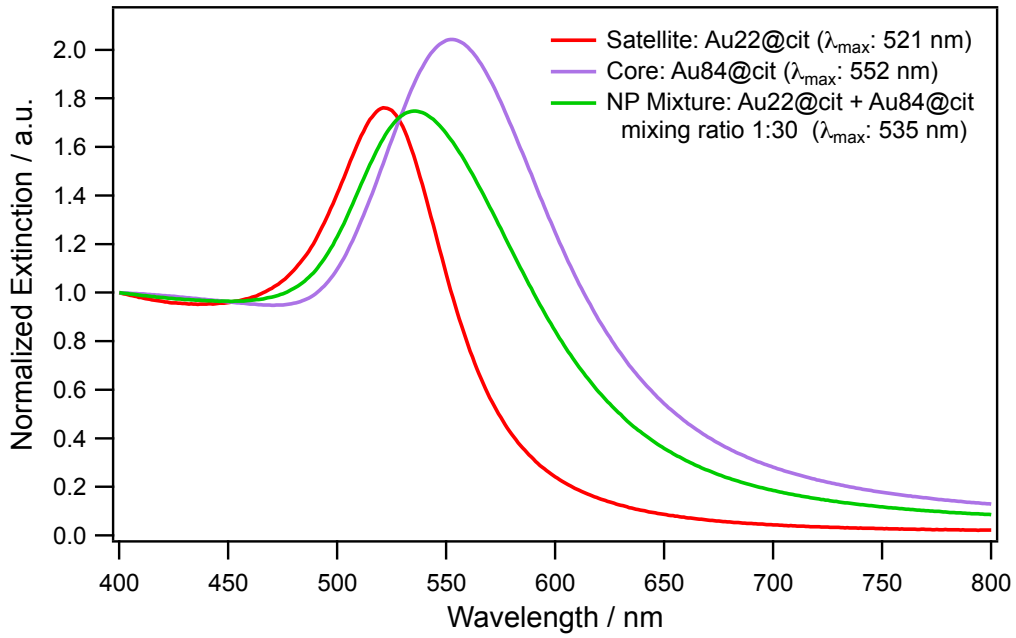

Figure S7: UV/vis spectra of citrate-stabilized AuNPs of (**A**) 22 nm (red) and (**B**) 84 nm in diameter (purple). (**C**) Mixture of large and small NPs in 1:30 mixing ratio (green).

SAXS Characterization and Three-Dimensional Modeling

The core as well as the satellite NPs could be perfectly fit with a simple model of a homogenous sphere (**Figure S8A,B**). In case of the BSA-stabilized satellites, the protein was not considered in the model as it exhibits a negligible scattering contrast compared to gold.

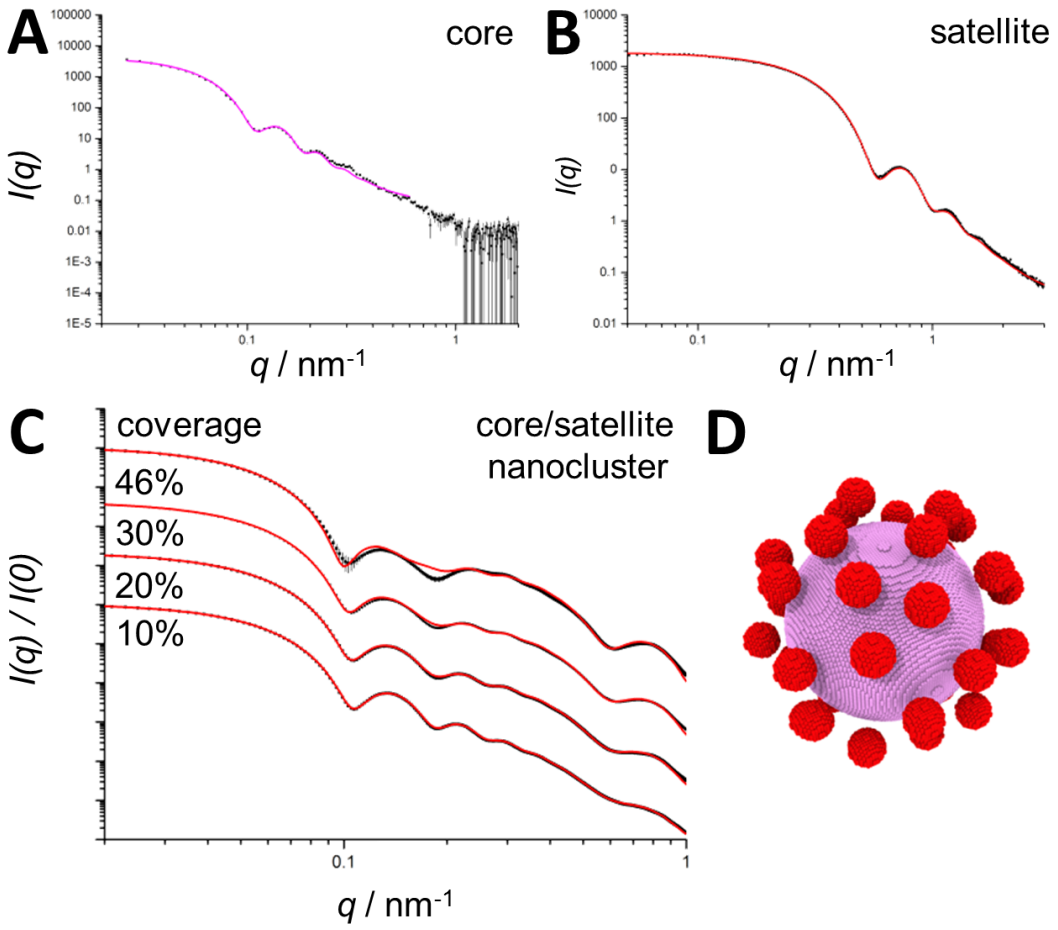

Figure S8: SAXS characterization of the individual building blocks: (**A**) core particles with an average radius of 42 ± 4 nm and (**B**) satellite particles with an average radius of 7.5 ± 0.9 nm. (**C**) Comparison of the scattering of the three-dimensional core/satellite nanocluster model (in red) and the analytical expression[6] for Pickering-type emulsions (in black) with different values of Au on Au coverage: 10%, 20%, 30%, and 46% (jamming limit). For comparison and better visibility, the curves have been normalized with respect to their forward scattering $I(0)$ and offset. (**D**) Schematic representation of the three-dimensional model of a Au84/Au16 core/satellite nanocluster consisting of >50,000 scattering centers.

In order to account for the scattering contribution that arises from the correlation of the small satellites with each other we had to use a three-dimensional model approach. The analytical model[6] for Pickering-type emulsions become more and more inaccurate with increasing coverage, as it cannot capture this scattering contribution. See **Figure S8C** for a direct comparison of the analytical and three-dimensional model generated scattering curves. In both cases the dispersity in size of the satellites was not included as this would have meant an exceptional higher computing time and also a much more sophisticated model that would have to account for the fact that adsorption energy is proportional to R^2 and would lead to the preferential adsorption of larger particles. Therefore, the models we used are only valid if the satellites have a low dispersity in size, which is the case. It can clearly be seen that at low coverage both approaches yield the same result but when the coverage increases beyond 20%, the correlation of the satellites starts to show and the analytical model starts to deviate from the three-dimensional model considerably. The system we investigated is close to the jamming limit and therefore we decided to use the three-dimensional model approach.

This was done in the following way. First, the number of attached spheres is calculated from the specified sizes of core and satellite, the amount of coverage as well as the shell size from the protein (BSA). Then, a user specified number of points that serve as scattering centers are used to build up the core and the satellite (see **Figure S8D**). In order to mimic the random sequential adsorption of the small spheres on the core, our software randomly sets satellites on the core and checks if the position is overlapping with any already present satellites and discards them if that is the case to set a new one. This is repeated until the calculated number of satellites is reached or until no more spheres can be set over 10,000 times, which corresponds to the jamming limit. Because the scattering of the samples is the average of all clusters and therefore of many satellite configurations, we had to calculate a certain number of such clusters to account for that. We also introduced dispersity in size of the core into this approach by calculating a Gaussian distribution of core sizes with the dispersity in size from the fitting of the cores alone. We found that the best compromise between resolution of the data and calculation time was to take 13 different core sizes and for each of these to generate 10 different clusters with the random sequential adsorption to a total of 130 clusters for each scattering curve. More samples do not significantly alter the quality (error bars) of the calculated scattering curves and the same goes for the number

of sizes. In order to get one scattering curve from the 130 clusters each of the individual scattering curves was weighted with the Gaussian size distribution and the cluster volume. These weighted scattering curves were averaged to yield the final scattering curve representing the sample. In a last step this averaged curve was smeared with the instrumental broadening arising from our pinhole setup by convolution with a series of Gaussians that takes into account that at different detector distances the amount of smearing differs. The scattering curve for each calculated cluster was calculated using the program *Debyer* (https://github.com/wojdyr/debyer) at its core it uses the Debye equation:

$$I(q) = \sum_i \sum_j f_i f_j \frac{\sin(q r_{ij})}{q r_{ij}} \qquad \text{Eq. S1}$$

with q being the scattering vector, r_{ij} as the distance between scattering centers i and j, and f_i as the atomic scattering factor for the ith atom, which is also a function of q – but for the sake of readability, this was omitted in the formula notation.

The smeared curve was then normalized with respect to $I(0)$ with the experimental data. The best fit was determined by a systematic screening of a broad range of different core-satellite distances and satellite coverages by a brute-force search. The best fitting calculated scattering spectrum was determined by the lowest mean squared error (MSE) in comparison to the experiment within the q-values of the cluster area (as defined in **Figure 3** in the main text article). The standard deviation of the results was defined as a 10% deviation of the best possible fit to the experiment (lowest MSE).

The main challenge in modelling of SAXS scattering of nanoclusters is that the q-range characteristic for the interaction of the building blocks is a convolution of satellite number and interparticle distances. However, the SAXS results are in-line with the electromagnetic modelling and UV/vis experimental data. SAXS and UV/vis spectroscopy are highly sensitive methods for interparticle distances within NP arrangements, each based on independent physical scattering phenomena (X-rays, light/plasmonics). By combination of both data, the strong convolution of satellite number and core-to-satellite distances can be decoupled and evaluated. Our findings show that the ensemble-averaged core-to-satellite distance can be evaluated with very low uncertainty (<1nm). **Figure S9** shows that even small deviations within the range of 1 nm significantly change the signature of the respective q-range in the modelled SAXS data. We are confident that the evaluated ensemble-averaged values are in good agreement with the experimental findings.

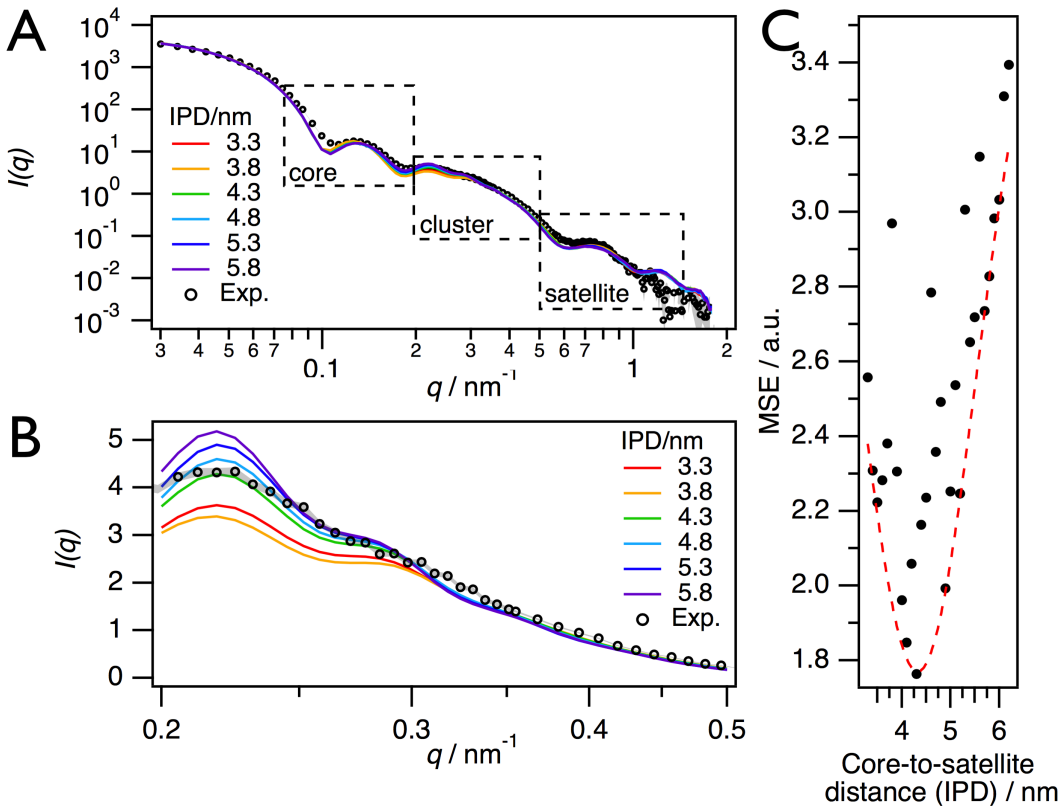

Figure S9: Sensitivity of SAXS for changes in core-to-satellite (IPD) distances at constant satellite coverage: (**A**) Experimental data of Au84/Au16 nanoclusters compared to a selection of three-dimensional models with IPDs between 3.3 and 5.8 nm. (**B**) Comparison of experimental and modeled scattering data in the *q*-range characteristic for core/satellite nanoclusters (0.2 to 0.5 nm^{-1}). (**C**) The quality of the modeling was based on the mean square error (MSE). The dashed red curve indicates the lower bound of the MSE as a guide to the eye. Best agreement was found for a core-to-satellite separation of 4.3 nm (see **Table 1** and **Table S2**).

Table S1: Structural composition of Au84/Au16 nanoclusters as characterized by UV/vis spectroscopy, SAXS, and the combination of both methods.

Method	UV/vis	SAXS	UV/vis + SAXS
Core radius /nm	42[a]	42 ± 4[b]	42
Satellite radius /nm	8[a]	7.5 ± 0.8[c]	8
Core-to-satellite distance /nm	--	4.3 ± 0.3[d]	4 ± 1[e]
Number of satellites per core	--	35 ± 1[d]	36 ± 2[e]

a) Evaluated based on electromagnetic modeling (**Figure S14**).
b) Variability in size of the core is based on a standard deviation of 0.08.
c) Variability in size of the satellites is based on a standard deviation of 0.10.
d) Variability in size of the satellites was omitted in the applied three-dimensional model.
e) Based on correlation on nanocluster structure and optical response (**Figure 5**).

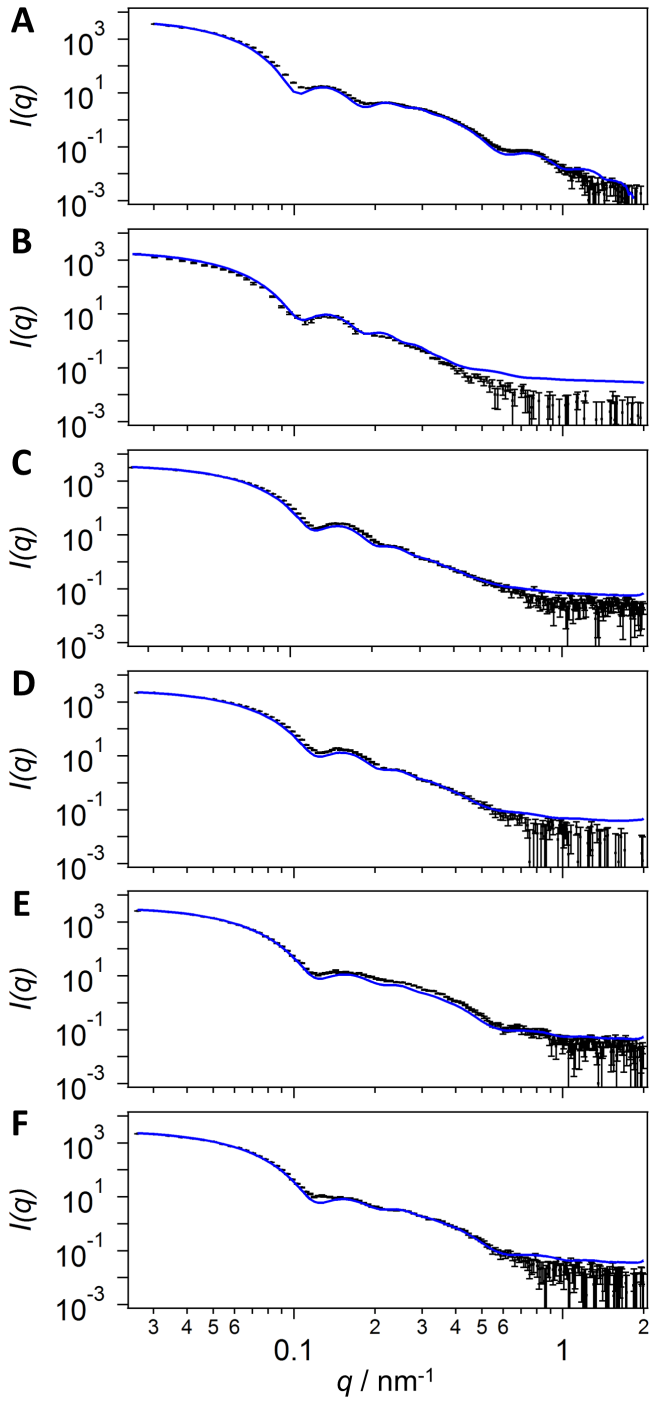

Figure S10: Characterization of the structural composition of different nanoclusters with different building block sizes, material compositions, and protein coatings *via* SAXS: The measured scattering spectra of the core-satellite nanoclusters (black curves) were fitted to a three-dimensional core/satellite model (blue curves). (**A**) Au84/Au16 (BSA) – **Figure 2B**; (**B**) Au84/Ag21 (BSA) – **Figure 2D**; (**C**) Au71/Au16 (CYTC) – **Figure S2A**; (**D**) Au71/Au16 (BLG) – **Figure S2B**; (**E**) Au71/Au16 (CYTC) – **Figure S2C**; (**F**) Au71/Au16 (BSA) – **Figure S2D**; (for exact building block sizes and further details see **Table S2**).

Table S2: Structural composition of different nanoclusters with different building block sizes, material compositions, and protein coatings as characterized by SAXS.

Radius of Au core NPs /nm[a]	42.0±3.4	42.0±3.4	35.3±3.9	35.3±3.9	35.3±3.9	35.3±3.9
Satellite material	Au	Ag	Au	Au	Au	Au
Radius of satellite NPs /nm[a]	7.5±0.8	10.5±1.2	7.6±0.8	7.9±0.9	7.5±0.8	7.2±0.8
Satellite coating	BSA	BSA	CYTC	BLG	CA	BSA
Core-to-satellite distance /nm[b]	4.3±0.3	4.0±0.4	6.7±0.2	6.8±0.2	6.7±0.7	6.2±0.5
Number of satellites per core[b]	35±1	11±1	3±1	7±1	22±2	23±1
Corresponding Figures	2B	2D	S2A	S2B	S2C	S2D

a) Variability in size is based on the standard deviation derived from a Gaussian distribution.

b) Variability in size of the satellites was omitted in the applied three-dimensional modeling of SAXS data. The given errors indicate the uncertainty of the ensemble-averaged core-to-satellite distance and number of satellites per core, respectively.

For the nanoclusters formed using different proteins (**Table S2**, columns 3-6 and **Figure S2**), smaller cores of 35.3 ± 3.9 nm radius and satellites with radii ranging between 7.2-7.9 nm were employed. The SAXS results are highly consistent with the observations from electron microscopy and UV/vis spectroscopy (**Figure S2**) and confirm the differences in satellite coverage. The number of satellites per core particle is the lowest for CYTC, followed by BLG and CA, and being highest for BSA.

Optical Characterization and Electromagnetic Modeling

Ideally Symmetric Distribution of Satellites -- Simple Polygon Model

Assemblies with ideal symmetric satellite distributions were modeled as Platonic and Archimedean polyhedral (see selection in **Figure S11**). These polyhedral are ideal bodies to model satellite distributions with equidistant satellite-to-satellite separations. In addition, based on the high symmetry of these polyhedra, the calculation of rotationally averaged extinction spectra is facilitated. This simple model suffices well to describe nanocluster configurations with 4, 6, 8, 12, 20, 24, 30, and 60 satellites with equidistant satellite-to-satellite separations and constant core-to-satellite distances. This quantization results in the main shortcoming of this model namely the lack of configurations for variable numbers of satellites. In order to fill the gaps, interpolation is required to predict the optical characteristics of nanoclusters with 5, 7, 9, 11, 13-19, 21-23, 25-29, 31-59, 61 and above.

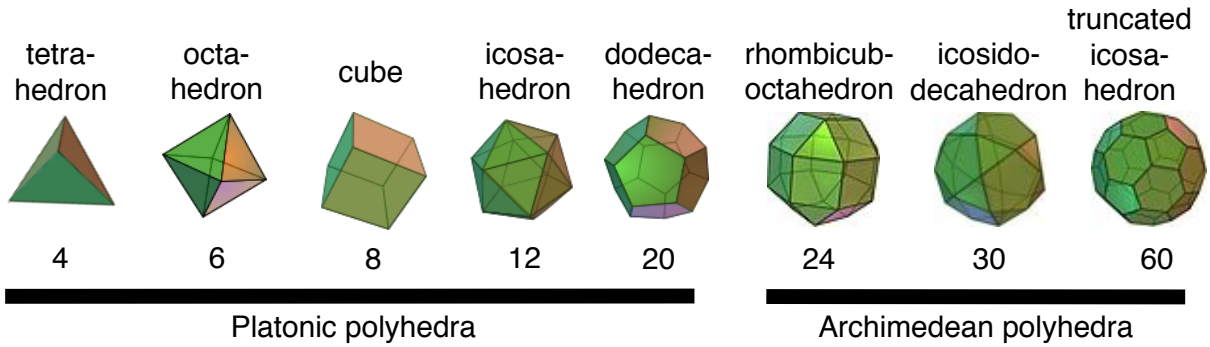

Figure S11: Polyhedra of different number of vertices used for modeling of core/satellite nanocluster morphologies with an ideally symmetric distribution of satellite particles around a core particle (located in the center of the polyhedra). Images are reproduced with permission under the terms of the *GNU Free Documentation License, Version 1.2* and under the *Creative Commons Attribution-Share Alike 3.0 Unported license* (CC BY-SA 3.0).

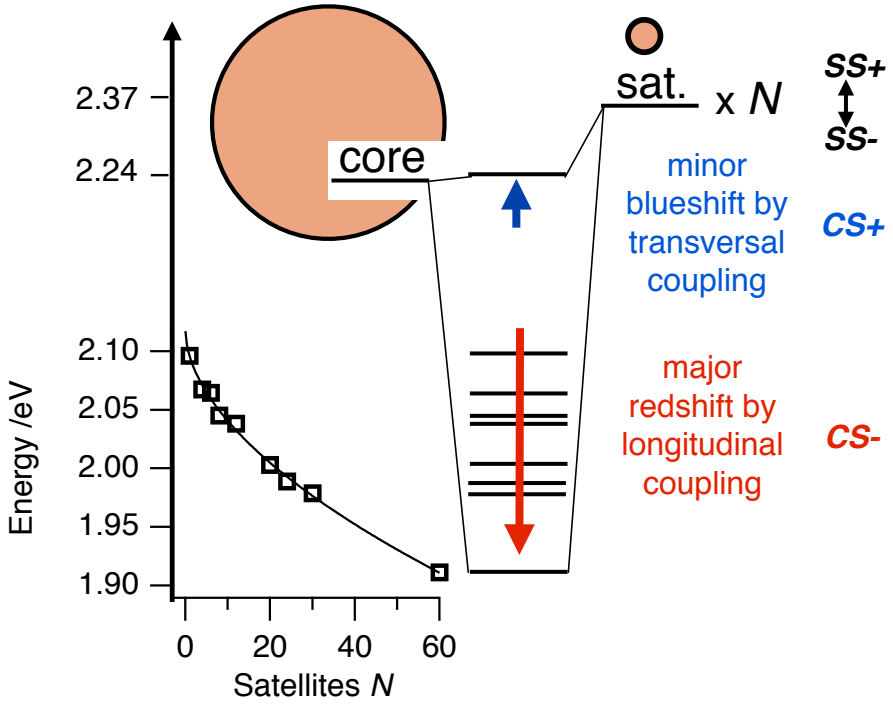

Figure S12: Hybridization model of a core/satellite nanocluster with an ideally symmetric distribution of satellite particles at the core surface. The energetic levels correspond to the localized surface plasmon resonances of the building blocks (gold core diameter 84 nm; gold satellite diameter 16 nm) and the dominant radiant mode of the core/satellite nanoclusters with equidistant core-to-satellite separations of 2 nm in water. With increasing number of satellite particles *N*, the radiant mode experiences a major red shift toward lower energies (similar to the longitudinal coupling in a heterodimer of the building blocks; CS-) resulting form core-satellite coupling (CS). Additionally, the nonradiant mode arises blue-shifted at higher energies compared to the core particle (similar to the transversal coupling in a heterodimer of the building blocks; CS+). This blue shift is less pronounced and can hardly be evaluated from the extinction spectra owing to its strong overlap with the dominant radiant mode. To be precise, the energetic levels of the individual satellite particles cannot be expected to be completely degenerated. Especially at higher numbers of satellites, that is for closer satellite-to-satellite distances, intersatellite coupling (SS) results in energetic splitting. Thus, some satellite particles are shifted to lower energies (similar to the longitudinal coupling in a homodimer of satellites; SS-) and others are shifted to higher energies (similar to the transversal coupling in a homodimer of satellites; SS+). This splitting should result in a broadening of the nonradiant.

Surface Charge Distributions of Core/Satellite Nanoclusters

The surface change distributions were calculated from the modeled electric fields at nanometer resolution. **Figure S13** shows a selection of surface charge distribution with different spatial integrations of the surface charge density calculated from the gradient of the electric field and normalized for better visibility.

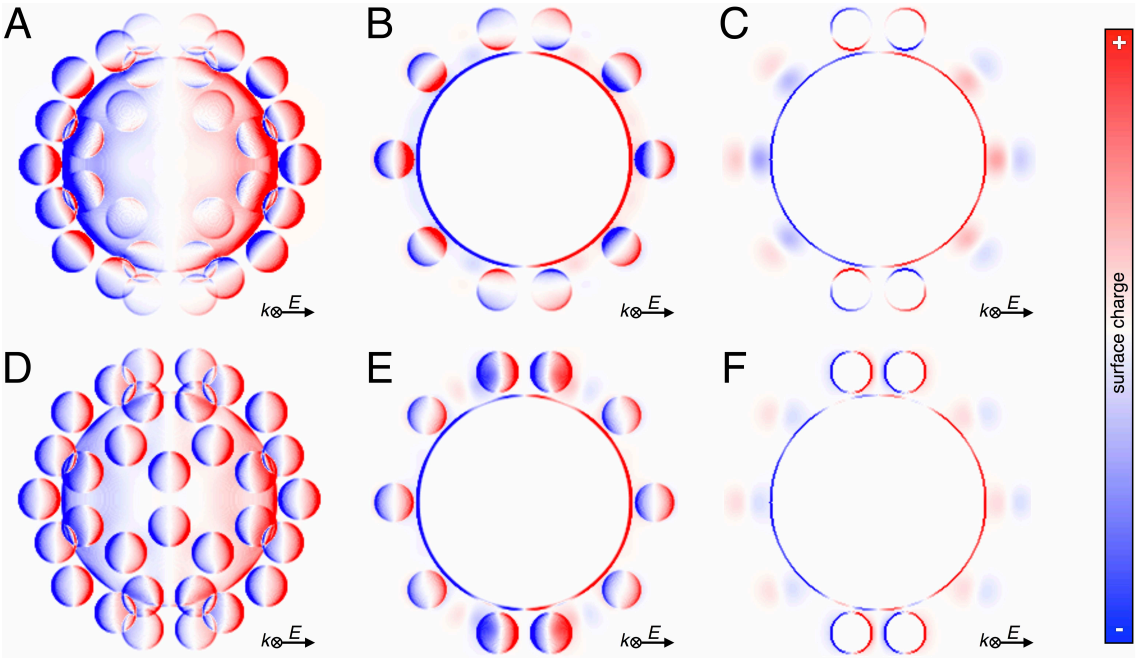

Figure S13: Modeled surface charge distributions of a Au84/Au16 core/satellite nanocluster with an ideally symmetric distribution of satellite particles at the core surface (gold core diameter 84 nm; gold satellite diameter 16 nm) with equidistant core-to-satellite separations of 2 nm in water. The surface charge distribution was calculated from the gradient of the electric normalized for the sake of visibility. The radiant mode (**A,B,C**) and nonradiant mode (**D,E,F**) are shown for different types of integration along the wave vector *k*: (**A,D**) Integration over the complete nanocluster; (**B,E**) Integration in a reduced volume of +- one satellite radius from the center plane of the nanocluster perpendicular to *k*; and (**C,F**) Integration as cross-section of 1 nm in thickness at the center plane of the nanocluster perpendicular to *k*. Subfigures **A,B,C** clearly show that in the radiant resonance results from strong core-to-satellite coupling. All satellite particles are oriented toward the core surface based on the dominant dipolar polarization of the core particle. In the nonradiant regime (**D,E,F**), the satellite particles are directly polarized by the external electric field.

Comparison of the Simulated and the Experimental Extinction of the Building Blocks

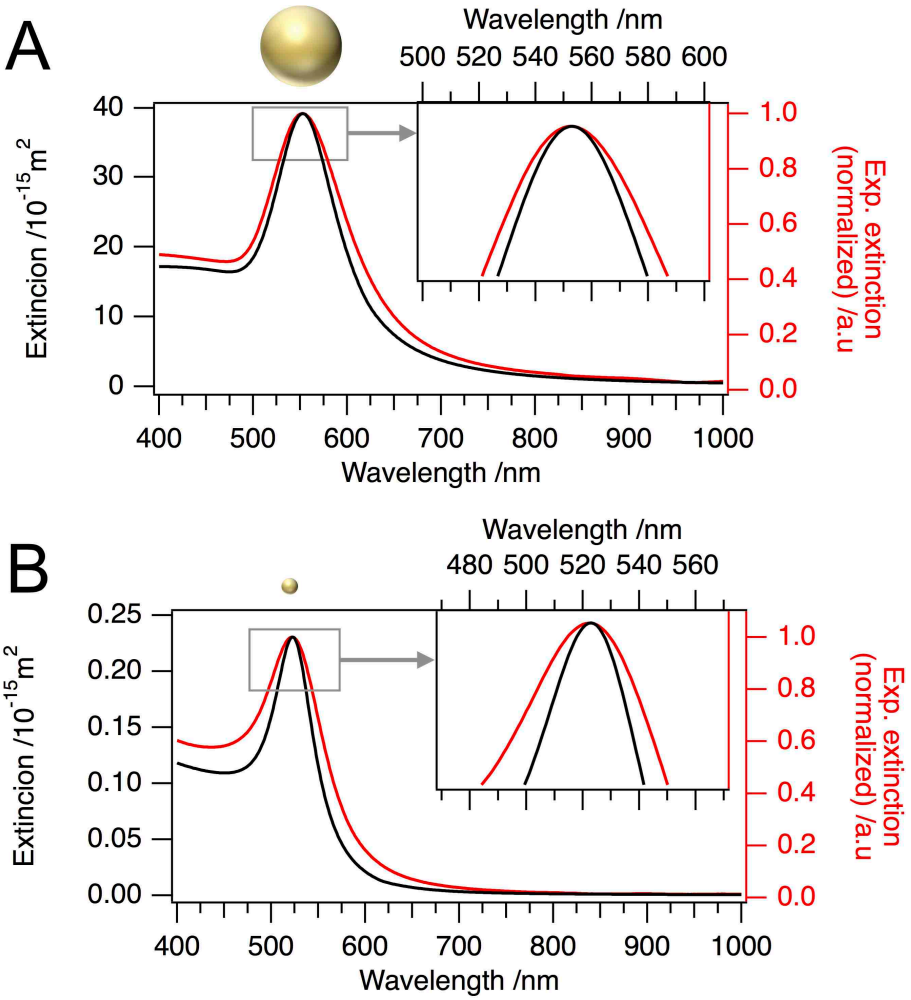

Figure S14: Modeled extinction cross-section (black, left axis) of an AuNP of (**A**) 84 nm and (**B**) 16 nm in diameter in water compared to the normalized experimental extinction (red, right axis) of the (**A**) Au core particles and (**B**) Au satellite particles used for core/satellite nanocluster assembly.

Random Distribution of Satellites – Random Sequential Adsorption Model

Assemblies with disordered satellite distribution were modeled based on an algorithm following a random sequential adsorption (RSA) mechanism. The RSA mechanism was based on the following steps: (1) A first satellite particle is randomly placed at the core surface with a distinct core-to-satellite separation. (2) The next satellite is placed randomly at the core surface. (3) The algorithm checks if there is an overlap of this new satellite with a satellite already existing at the core surface. If an overlap is found, the position of the new satellite is declined and the algorithm returns to step 2. If no overlap if found, the position of this satellite is accepted and the algorithm return to step 2 for the next satellite. The steps 2 and 3 are repeated until the given number of satellites is reached or the surface is fully saturated with satellites (*i.e.*, the jamming limit is reached). Please note that each satellite exhibits the same core-to-satellite separation and a minimum satellite-to-satellite separation of two times the core-to-satellite separation is maintained. The latter was chosen to emulate the presence of the protein coating around the satellite particles.

To account for the assembly variability, each morphological nanocluster species was represented by an ensemble calculated from ten randomly assembled configurations.

Influence of Changes in Refractive Index of the Medium on the Optical Response of Core/Satellite Nanoclusters and their Building Blocks

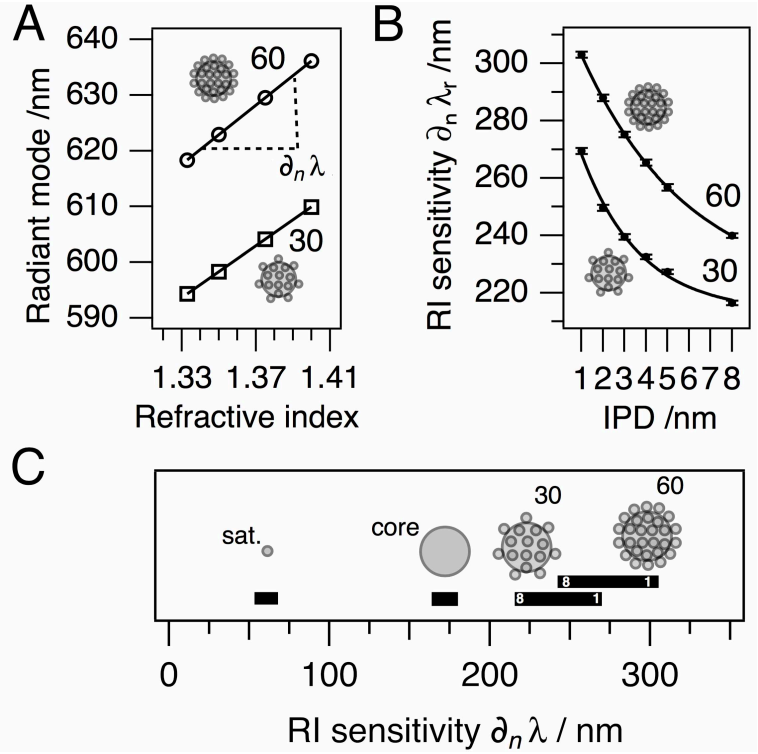

Figure S15: Modeled influence of changes in medium refractive index on the radiant mode of core/satellite nanoclusters with an ideally symmetric distribution of satellite particles (diameter 16 nm) at the surface of a core particle (diameter 84 nm). (**A**) The linear shift toward red for an increase in refractive index of the medium is shown for two gold/gold nanocluster configurations with core-to-satellite distances of 4 nm and 30 or 60 satellites particles. The slope of the linear regression $\partial_n \lambda$ is a measure of the effective sensitivity toward changes in refractive index (RI sensitivity; given in nm per refractive index unit). (**B**) Generalized for different core-to-satellite distances (IPD in nm), an allometric power low dependence can be found for the RI sensitivity on the interparticle distances. Nanocluster configurations with higher coverage of satellites exhibit higher sensitivity toward changes in refractive index of the medium. (**C**) RI sensitivity of two cluster configurations (30 and 60 satellites) compared to their building blocks (core diameter 84 nm; satellite diameter 16 nm). The black bars below the nanoclusters indicate the variability in RI sensitivity for changes in core-to-satellite distances between 1 nm and 8 nm. The black bars below the building blocks indicate the variability in RI sensitivity for changes in particle size to emulate nanoparticle polydispersity (10%).

Influence of the Size of the Core on the Optical Response of Core/Satellite Nanoclusters

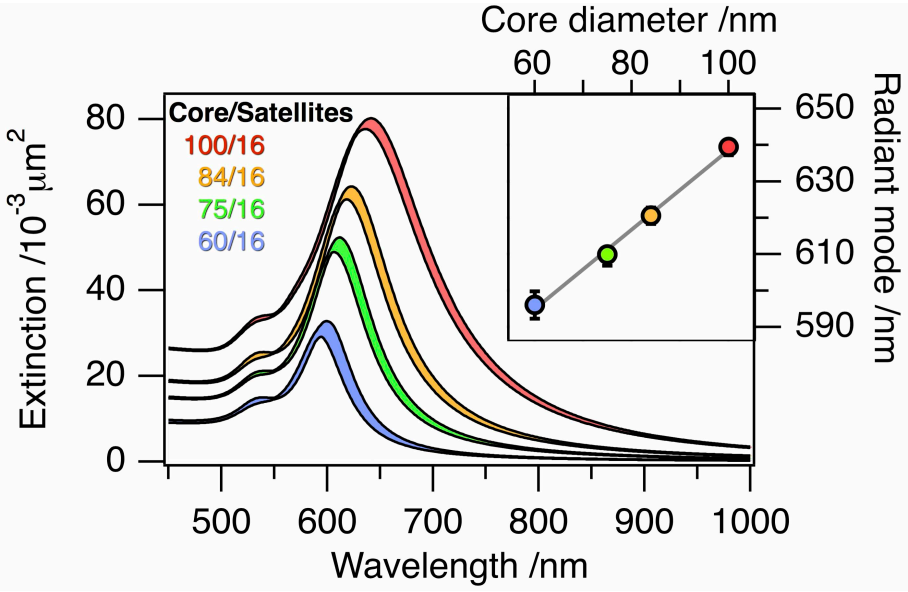

Figure S16: Modeled optical response of core/satellite nanoclusters consisting of Au core particles of variable sizes (diameter: 60 nm, 75 nm, 84 nm, and 100 nm) and randomly distributed satellite particles (diameter: 16 nm) at the jamming limit, *i.e.*, with a maximum number of satellite particles at the core surface. The core-to-satellite distance was set to 4 nm. The dominant radiant mode λ_r shifts linearly toward red with increasing diameter of the core particle D_{core}. The linear regression yields λ_r / nm = 529.5 + 1.1 D_{core} / nm. Thus, at the maximum coverage of satellites for which the most pronounced red-shift can be expected, a change of 10 nm in the effective diameter of the core particle corresponds to a red-shift of about 11 nm of the radiant mode.

Diffuse Reflectance UV/vis Spectroscopy

The absorption and scattering losses of nanocluster samples were determined using a UV/vis spectrophotometer Cary 5000 (Agilent Technologies Deutschland GmbH) equipped with the external diffuse reflectance accessory 2500 (integrating sphere). In the following, *I* represents the measured intensities and *T* denotes the transmittance of absorbed (A), scattered (S), and transmitted (T) light. A quartz glass cuvette was positioned at the center of the integrating sphere and a fixed set of measurements was performed: sample measured without light trap ($I_0 - I_A = I_S + I_T$); sample measured with light trap ($I_S = I_0\ T_S\ (1\text{-}T_A)$); and Milli-Q water measured without light trap as background (I_0). From this data, the absorption and scattering losses were evaluated. First, we determine the intensity of the transmitted light (I_T) by subtraction of the "sample with light trap" data (I_S) from the "sample without light trap" data ($I_0 - I_A$).

$$I_T = I_0 - I_A - I_S \qquad \text{Eq. S2}$$

Similarly, the intensity of absorbed light (I_A) is calculated by subtraction of both the "sample without light trap" data, which is the combined intensity of scattered and transmitted light ($I_S + I_T$), and the intensity of transmitted light I_T from the "background" intensity (I_0).

$$I_A = I_0 - I_S - I_T \qquad \text{Eq. S3}$$

The transmittance of the absorbed light (T_A) is given by the ratio of the intensity of absorbed light (I_A) to the "background" intensity (I_0).

$$T_A = I_A / I_0 \qquad \text{Eq. S4}$$

The transmittance of the scattered light (T_S) can be determined from the "sample with light trap" data ($I_S = I_0\ T_S\ (1\text{-}T_A)$) using the "background" intensity (I_0) and the transmittance of the absorbed light (T_A).

$$T_S = I_S / (I_0\ (1\text{-}T_A)) \qquad \text{Eq. S5}$$

Finally, the transmittance of the total extinct light (T_E) is given by the sum of the transmittance of absorbed (T_A) and scattered light (T_S).

$$T_E = T_A + T_S \qquad \text{Eq. S6}$$

References

1. Righetti, P. G.; Caravaggio, T. Isoelectric Points and Molecular Weights of Proteins: A Table. *J. Chromatogr. A* **1976**, *127,* 1-28.
2. Williams, J.; Elleman, T. C.; Kingston, I. B.; Wilkins, A. G.; Kuhn, K. A. The Primary Structure of Hen Ovotransferrin. *Eur. J. Biochem.* **1982**, *122,* 297-303.
3. Strozyk, M. S.; Chanana, M.; Pastoriza-Santos, I.; Pérez-Juste, J.; Liz-Marzán, L. M. Protein/Polymer-Based Dual-Responsive Gold Nanoparticles with pH-Dependent Thermal Sensitivity. *Adv. Funct. Mater.* **2012**, *22,* 1436-1444.
4. Chanana, M.; Correa-Duarte, M. A.; Liz-Marzán, L. M. Insulin-Coated Gold Nanoparticles: A Plasmonic Device for Studying Metal–Protein Interactions. *Small* **2011**, *7,* 2650-2660.
5. Dewald, I.; Isakin, O.; Schubert, J.; Kraus, T.; Chanana, M. Protein Identity and Environmental Parameters Determine the Final Physico-Chemical Properties of Protein-Coated Metal Nanoparticles. *J. Phys. Chem. C* **2015**, *119,* 25482-25492.
6. Larson-Smith, K.; Jackson, A.; Pozzo, D. C. Small Angle Scattering Model for Pickering Emulsions and Raspberry Particles. *J. Colloid Interface Sci.* **2010**, *343,* 36-41.